Slab stagnation in the shallow lower mantle linked to an increase in mantle viscosity

Hauke Marquardt[1]★[†] and Lowell Miyagi[2]

Subduction of oceanic lithosphere is the main process by which material from Earth's surface and atmosphere is recycled back into the deep mantle. Seismic images indicate that subducting slabs of oceanic lithosphere can stagnate and broaden in the shallow lower mantle[1,2]. The main phases of the lower mantle, bridgmanite and ferropericlase, do not show any structural transitions at these depths, so only moderate and smooth viscosity variations are expected with depth[3,4] to at least ~2,500 km. The reason for slab stagnation, which may also lead to the formation of chemically distinct reservoirs in Earth's deep mantle[5], is therefore unclear. Here we use synchrotron radial X-ray diffraction to measure *in situ* the deformation behaviour of ferropericlase at pressures of up to 96 GPa. We find that the strength of ferropericlase increases by a factor of three at pressures from 20 to 65 GPa. Modelling based on our experimental data shows that the viscosity in the region surrounding the subducting slabs could increase by 2.3 orders of magnitude throughout the upper 900 km of the lower mantle. Such a strong increase in viscosity can lead to the stagnation of slabs that are sinking through the shallow lower mantle.

The Earth's lower mantle, ranging from 660 km to 2,890 km depth, constitutes more than 50% of Earth's volume and is the largest geochemical reservoir for many elements. Throughout Earth's history, substantial amounts of material have been exchanged between the deep mantle and Earth's surface and atmosphere. Material transport from Earth's surface into the deep mantle occurs by subduction of oceanic lithosphere. Historically, many scientists favoured a model of separate mantle convection within the upper and lower mantle, but seismology[6,7], mantle dynamic models[8] and petrology[9] provide evidence for subducting slabs penetrating the 660 km discontinuity and at least partial mixing between the upper and lower mantle. Recent seismic tomography studies suggest that in many subduction systems, such as under South America and Indonesia, slabs broaden and stagnate in the upper ~500–1,000 km of the lower mantle[1,2].

In high-strain regions of the lower mantle, such as near subducting slabs[10] and in boundary layers[11], (Mg,Fe)O ferropericlase—the rheologically weakest lower-mantle phase[3]—is likely to form an interconnected network[12]. In these conditions, the overall rheology will be dominated by ferropericlase even though $(Mg,Fe)SiO_3$ bridgmanite (silicate–perovskite) is volumetrically more abundant in the lower mantle[3,12,13]. Previous high-pressure deformation experiments on MgO and $(Mg_{0.83}Fe_{0.17})O$ concluded that the rheological behaviour of (Mg,Fe)O is essentially unchanged throughout the mantle[14,15]. In contrast to these experimental findings, an inversion of the energetically favoured slip system in MgO from $\langle 110 \rangle \{110\}$ to $\langle 110 \rangle \{100\}$ has been recently proposed to take place between 30 GPa and 60 GPa at 300 K on the basis of a multi-scale modelling approach[16].

Here, we performed angle-dispersive high-pressure radial X-ray diffraction (rXRD) on powders of $(Mg_{0.9}Fe_{0.1})O$ and $(Mg_{0.8}Fe_{0.2})O$ at Beamline 12.2.2 of the Advanced Light Source, Lawrence Berkeley National Laboratory. Two runs were performed in the diamond-anvil cell (DAC) with a very fine pressure resolution to a maximum pressure of 83 GPa using X-ray transparent cubic boron nitride (cBN) gaskets. A third run was performed in a Be gasket to 96 GPa. All data were analysed for unit-cell parameters, elastic strains and texture (see Supplementary Information). A representative analysis is shown in Supplementary Fig. 1.

From our experiments, we derive differential elastic lattice strains. We observe an initial increase of all lattice strains $Q(hkl)$, where *hkl* refer to the Miller indices of the respective lattice planes. This initial increase is followed by a saturation above roughly 10 GPa (Fig. 1), indicating that plastic flow was achieved. Starting from 20 to 30 GPa, our data show a second increase of all lattice strains up to pressures of ~60 GPa. Over this pressure range, we observe increases of 2–2.5 times for $Q(111)$, $Q(220)$ and $Q(311)$, but only a slight change for $Q(200)$. This pressure range is consistent with the pressure region of 30–60 GPa where changing slip system activities have been proposed for MgO by modelling[16]. In the following, we refer to the pressure range of increasing lattice strains as a 'rheology transition'.

From our data, we calculated the flow strength t (Fig. 2), which can be defined as $6\langle Q(hkl)\rangle G$, under the assumption that the stress state in the DAC was large enough to cause plastic flow of the sample[14]. Here, $\langle Q(hkl)\rangle$ refers to the arithmetic average of measured lattice strains and G is the high-pressure shear modulus (Reuss bound), taken from a previous high-pressure Brillouin scattering experiment on $(Mg_{0.9}Fe_{0.1})O$ (ref. 17). At pressures below 20 GPa, the strength that we observe for ferropericlase is in agreement with previous rXRD studies on (Mg,Fe)O (refs 15,18). However, between 20 GPa and 65 GPa, we observe a pronounced increase in ferropericlase strength, reflecting the increase of lattice strains. Our data suggest a strength of ferropericlase that is almost four times larger at pressures of the Earth's lowermost mantle than expected based on the previous report[15]. The increase of strength by a factor of three that we observe between 20 GPa and 65 GPa is consistent with the modelling results of critical resolved shear stresses (CRSS) in MgO, indicating changing slip system activities[16]. However, we note that based on our experiments alone, we cannot conclusively link our observation of increasing strength to a change of slip system activities. The increase of strength that we report here is also visible in a previous rXRD study on

[1]GFZ German Research Centre for Geosciences, Telegrafenberg, 14473 Potsdam, Germany. [2]University of Utah, 115 So. 1460 E., Salt Lake City, Utah 84112-0111, USA. [†]Present address: Bayerisches Geoinstitut BGI, University of Bayreuth, 95440 Bayreuth, Germany.
*e-mail: Hauke.Marquardt@uni-bayreuth.de
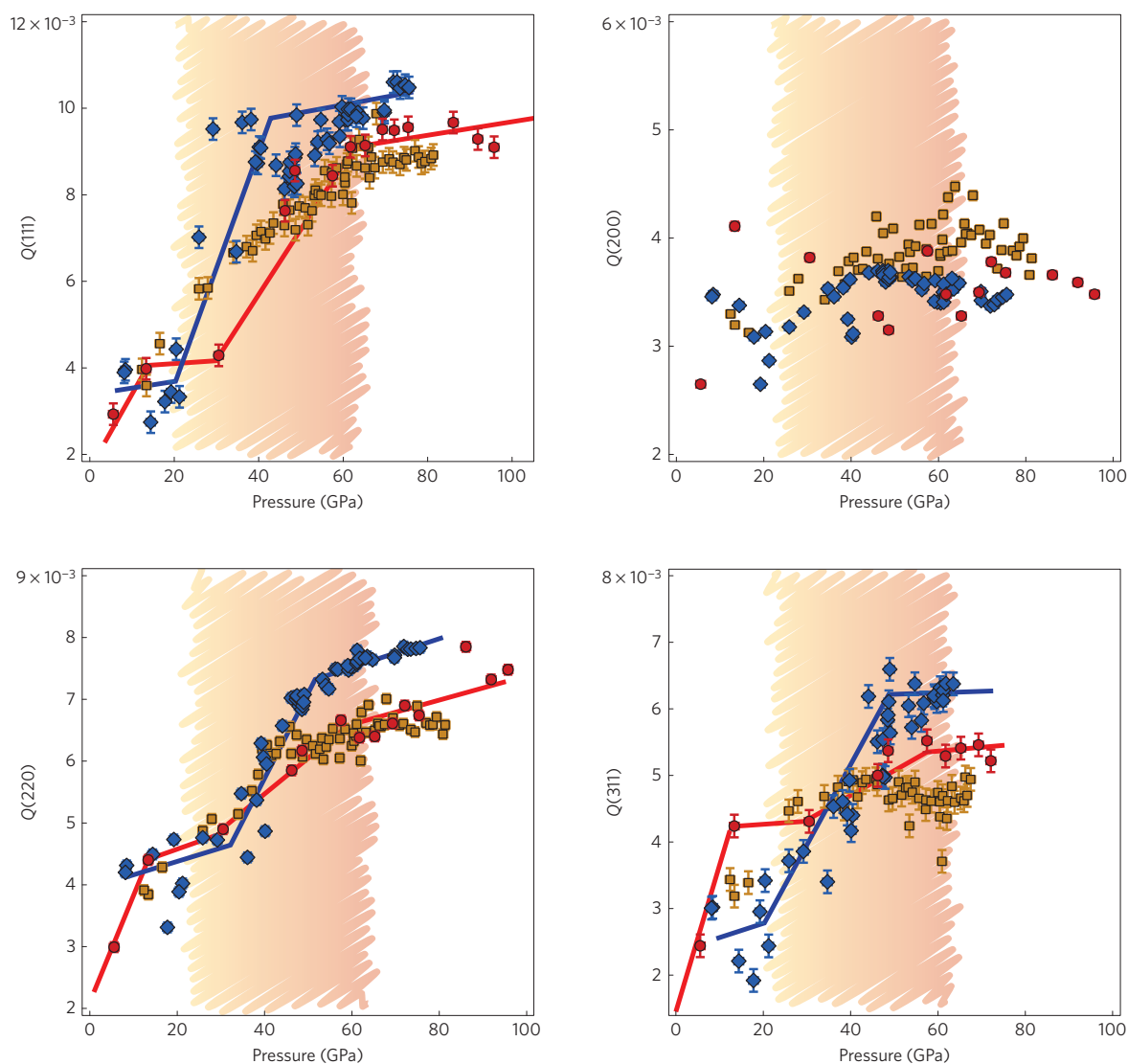
Figure 1 | Lattice strains in Q(111), Q(200), Q(220) and Q(311) measured in (Mg$_{0.8}$Fe$_{0.2}$)O and (Mg$_{0.9}$Fe$_{0.1}$)O ferropericlase. Red circles, (Mg$_{0.8}$Fe$_{0.2}$)O in Be-gasket; blue diamonds, (Mg$_{0.8}$Fe$_{0.2}$)O in cBN-gasket; orange squares, (Mg$_{0.9}$Fe$_{0.1}$)O in cBN-gasket. Error bars reflect uncertainties of Rietveld fit provided by the program MAUD. The solid lines are schematic representations of the observed trends for (Mg$_{0.8}$Fe$_{0.2}$)O. The hatched regions illustrate the pressure range of lattice strain increase. Lattice strains are dimensionless.

(Mg$_{0.4}$Fe$_{0.6}$)O (ref. 18), but was not recognized because of the limited experimental pressure range (Fig. 2). In contrast to the earlier study[15] on (Mg$_{0.83}$Fe$_{0.17}$)O, we do not observe a significant decrease of strength across the iron spin crossover that starts at around 60 GPa for our (Mg$_{0.8}$Fe$_{0.2}$)O sample (Supplementary Fig. 3). The discrepancy between our results and the earlier study[15] on (Mg$_{0.83}$Fe$_{0.17}$)O is probably related to the experimental limitations in the previous study, which was performed in energy dispersive mode with a single-element detector. This experimental set-up is not ideal for lattice strain or texture measurements owing to limited azimuthal resolution and coverage. We note that, in the present study, three experimental runs with different gasket materials and varying compression rates show highly consistent results. Figure 2 shows previously collected data points at combined high pressure and high temperature for comparison[19]. As expected, increasing temperature leads to a general decrease in strength. The increase of strength found here at 300 K can also be observed in the high-temperature data at 770 K, indicating that the rheology transition takes place in approximately the same pressure range at elevated temperatures. To calculate strength from the lattice strains measured

at high pressure/high temperature, we used a previous model for the shear modulus at high temperatures[17].

The increasing strength of ferropericlase throughout the rheology transition will increase mantle viscosity in high-strain regions, where ferropericlase forms an interconnected network[3,12,13]. Note that the elastic anisotropy of ferropericlase is small in the shallow lower mantle[20] and large deformation of ferropericlase would not produce detectable seismic anisotropy in this region. We used our experimental data for the strength of ferropericlase to calculate a lower-mantle viscosity profile using previously developed models that allow us to extrapolate room-temperature, high-strain measurements to lower-mantle conditions (see Supplementary Information). We note that the high-strain rates inherent to any experimental deformation study need to be extrapolated to geophysically relevant strain rates, which can introduce uncertainties, as indicated by a modelling study on MgO (ref. 21). Our model shows a strong increase of lower-mantle viscosity by 2.3 ± 0.3 orders of magnitude in the upper 900 km of the lower mantle, where the rheology transition takes place (Fig. 3 and Supplementary Fig. 5). At depths >1,500 km, the change of viscosity with depth becomes smaller.
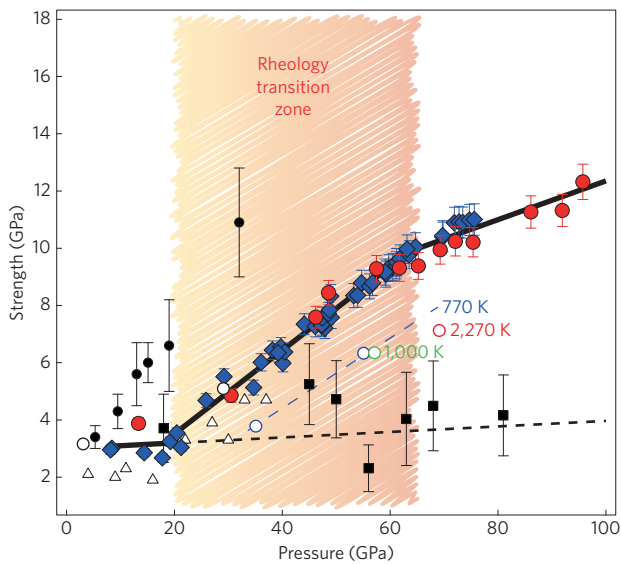
Figure 2 | Strength of (Mg$_{0.8}$Fe$_{0.2}$)O ferropericlase. Red circles, measurements in Be-gasket; blue diamonds, measurements in cBN gasket. Error bars include fitting uncertainties in $Q(hkl)$ and uncertainties in the high-pressure shear modulus. Solid black lines, linear fits to data in the pressure ranges <20 GPa, 20–65 GPa and >65 GPa. Dashed black line, linear extrapolation of data at pressures <20 GPa. Black squares, (Mg$_{0.83}$Fe$_{0.17}$)O (ref. 15), where calculation of flow strength from reported Q-values was performed using the shear modulus of ref. 17. White triangles, (Mg$_{0.4}$Fe$_{0.6}$)O (ref. 18). White circles, blue dashed line, (Mg$_{0.8}$Fe$_{0.2}$)O (ref. 19). Black circles, (Mg$_{0.9}$Fe$_{0.1}$)SiO$_3$ bridgmanite (ref. 29).

Below 1,800 km depth, the iron spin crossover in ferropericlase may lead to a reduction in mantle viscosity as a result of enhanced element diffusion rates[22] (see Supplementary Information).

The effect of a hypothetical mid-mantle viscosity hill on the fate of subducted slabs has been previously tested by numerical modelling[23], even though the underlying principle was not known. This study showed that a viscosity increase by a factor of 100, consistent with the viscosity increase inferred here, profoundly affects the fate of subducted slabs and in many scenarios leads to slab stagnation. The viscosity increase may also cause slab thickening or buckling[24]. In the uppermost lower mantle, the interior of the slab may be in a relatively low-strain state, but as it begins to thicken or buckle in response to the increasing viscosity in the surrounding mantle, the slab itself is likely to evolve to a high-strain state. This may lead to weakening of the slab through formation of an interconnected weak layer structure within the slab, further enhancing broadening and buckling.

A high probability for slabs to broaden and stagnate in the shallow lower mantle, as inferred from our data, can explain the seismic tomography observations under South America and Indonesia[1,2]. Our prediction is also supported by global, radially averaged seismic studies[25], including previous statistical analyses of a large number of tomographic models that show robust pattern changes at depth >1,500 km from dominant fast shear wave anomalies to dominant slow shear wave anomalies[26,27]. Furthermore, it is consistent with the need for a change in chemical (or thermal) state of the lower mantle at ~1,500 km depth to match mineral physics predictions and one-dimensional seismic models[28]. The impact of the inferred viscosity increase on descending slabs will depend on several factors, including the size, sinking speed and density of the slab. Slabs may therefore overcome the viscosity
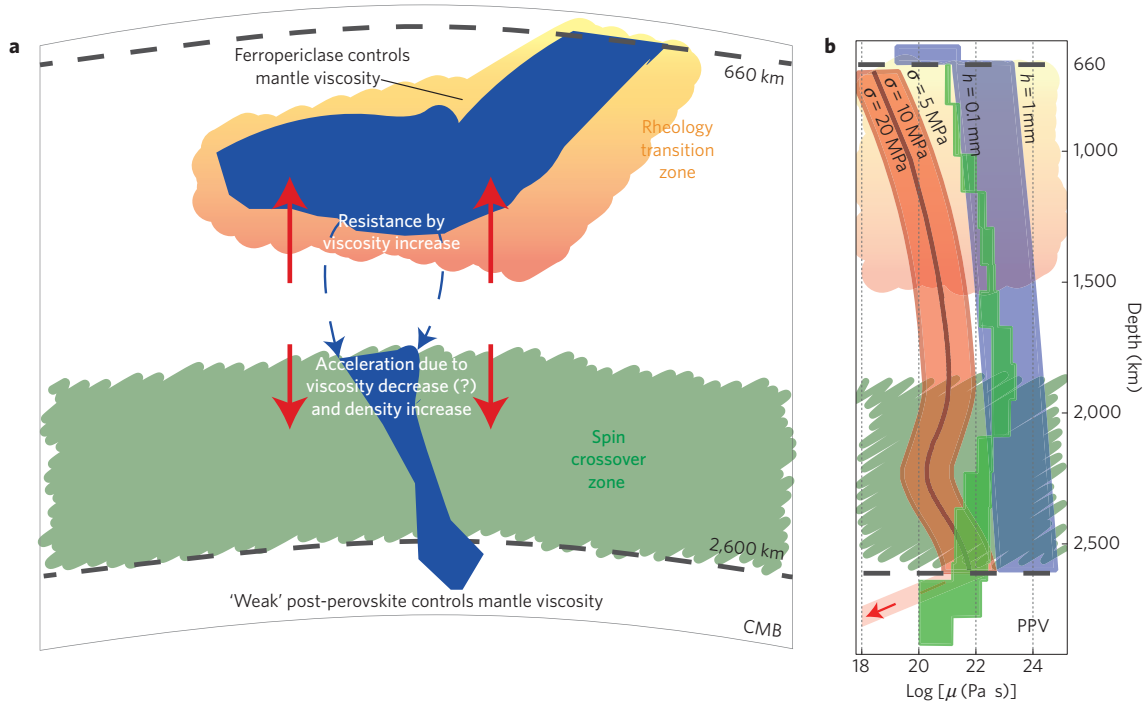
Figure 3 | Subducting slab in the lower mantle and effective viscosity profiles. a, Cartoon of subducting slab in Earth's lower mantle. Blue, subducting slab. Blue arrows, the slab may overcome the viscosity barrier and continue to sink into the deeper lower mantle. Red arrows, illustration of the effects of the effective viscosity profile on the descending slab. CMB, core–mantle boundary. **b**, Effective viscosity (μ) profiles. Red: Modelled viscosity profile in high-strain regions calculated for three different stress values σ. The effect of the iron spin crossover was taken as the average between the bounds in Supplementary Fig. 5. Blue: Modelled viscosity profile in low-strain areas calculated for two different grain size values h. A viscosity jump of two orders of magnitude at 660 km was assumed. Weak post-perovskite (PPV) may lead to a decrease of mantle viscosity in high strain areas illustrated by the arrow in **b**. Green: Predicted viscosity profile based on joint inversion of convection and glacial isostatic adjustment data for comparison (ref. 30). PPV, post-perovskite.

barrier and continue to sink to the core–mantle boundary (CMB). However, even in this case, we predict that slabs will broaden in the shallow lower mantle and remain at depth <1,500 km for long times. Even though our absolute values for calculated viscosities depend much more on the chosen input parameters than does the depth-derivative, all of our models indicate a viscosity in the uppermost lower mantle that is smaller than estimations for mantle viscosity in low-strain regions[3,4] (Fig. 3 and Supplementary Table 1). Therefore, our findings may not only provide a mechanism to stop the descent of slabs in the shallow lower mantle, but furthermore suggest a reduction of viscosity contrast at the 660 km discontinuity, which would allow slabs to enter the lower mantle in the first place.

Figure 3 summarizes a plausible scenario, where slabs slow down and broaden in response to the viscosity increase in the shallow lower mantle, but (part of) a slab may overcome the viscosity barrier and further descend into the lower mantle. Once it reaches the depth where the iron spin crossover in ferropericlase takes place, the slab may accelerate, because mantle viscosity decreases and low-spin ferropericlase makes the slab denser (at a faster rate than the surrounding mantle, because of the temperature dependence of the spin crossover[22]). Towards the CMB, a rheologically weak post-perovskite, as predicted by computations (and increasing temperatures), may further reduce mantle viscosity[4].

Our data provide a direct indication from mineral physics for a rheology transition in the lower mantle. The increase of viscosity caused by the rheology transition in ferropericlase is presumably reversible on changes in pressure and thus unrelated to the past history of mantle convection. It can, therefore, provide a mechanism that leads to broadening and stagnation (or at least long residence time) of slabs in the shallow lower mantle and can produce distinct geochemical reservoirs in Earth's lower mantle that remain mostly unmixed over geologic time. Such a mechanism may explain the geochemical differences between ocean island basalts (OIB) and mid-ocean ridge basalts (MORB) that point towards the existence of different distinct geochemical reservoirs in Earth's mantle[5].

References

1. Fukao, Y. & Obayashi, M. Subducted slabs stagnant above, penetrating through, and trapped below the 660 km discontinuity. *J. Geophys. Res.* **118,** 5920–5938 (2013).
2. Li, C., van der Hilst, R. D., Engdahl, E. R. & Burdick, S. A new global model for P wave speed variations in Earth's mantle. *Geochem. Geophys. Geosys.* **9,** Q05018 (2008).
3. Yamazaki, D. & Karato, S-i. Some mineral physics constraints on the rheology and geothermal structure of Earth's lower mantle. *Am. Mineral.* **86,** 385–391 (2001).
4. Ammann, M. W., Brodholt, J. P., Wookey, J. & Dobson, D. P. First-principles constraints on diffusion in lower-mantle minerals and a weak D″ layer. *Nature* **465,** 462–465 (2010).
5. Hofmann, A. W. Mantle geochemistry: The message from oceanic volcanism. *Nature* **385,** 219–229 (1997).
6. Van der Hilst, R. D., Widiyantoro, S. & Engdahl, E. R. Evidence for deep mantle circulation from global tomography. *Nature* **386,** 578–584 (1997).
7. Grand, S. P. Mantle shear structure beneath the Americas and surrounding oceans. *J. Geophys. Res.* **99,** 11591–11621 (1994).
8. Tackley, P. J. Mantle convection and plate tectonics: Toward an integrated physical and chemical theory. *Science* **288,** 2002–2007 (2000).
9. Walter, M. J. *et al.* Deep mantle cycling of oceanic crust: Evidence from diamonds and their mineral inclusions. *Science* **334,** 54–57 (2011).
10. Faccenda, M. Mid mantle seismic anisotropy around subduction zones. *Phys. Earth Planet. Inter.* **227,** 1–19 (2014).
11. McNamara, A. K., van Keken, P. E. & Karato, S-I. Development of anisotropic structure in the Earth's lower mantle by solid-state convection. *Nature* **416,** 310–314 (2002).
12. Yamazaki, D., Yoshino, T., Matsuzaki, T., Katsura, T. & Yoneda, A. Texture of (Mg,Fe)SiO$_3$ perovskite and ferro-periclase aggregate: Implications for rheology of the lower mantle. *Phys. Earth Planet. Inter.* **174,** 138–144 (2009).
13. Takeda, Y-T. Flow in rocks modelled as multiphase continua: Application to polymineralic rocks. *J. Struct. Geol.* **20,** 1569–1578 (1998).
14. Merkel, S. *et al.* Deformation of polycrystalline MgO at pressures of the lower mantle. *J. Geophys. Res.* **107(B11),** 2271 (2002).
15. Lin, J-F. *et al.* Deformation of lower-mantle ferropericlase (Mg,Fe)O across the electronic spin transition. *Phys. Chem. Miner.* **36,** 585–592 (2009).
16. Amodeo, J., Carrez, P. & Cordier, P. Modelling the effect of pressure on the critical shear stress of MgO single crystals. *Philos. Mag.* **92,** 1523–1541 (2012).
17. Marquardt, H., Speziale, S., Reichmann, H. J., Frost, D. J. & Schilling, F. R. Single-crystal elasticity of (Mg$_{0.9}$Fe$_{0.1}$)O to 81 GPa. *Earth Planet. Sci. Lett.* **287,** 345–352 (2009).
18. Tommaseo, C., Devine, J., Merkel, S., Speziale, S. & Wenk, H-R. Texture development and elastic stresses in magnesiowüstite at high pressure. *Phys. Chem. Miner.* **33,** 84–97 (2006).
19. Miyagi, L. *et al.* Combined resistive and laser heating technique for *in situ* radial X-ray diffraction in the diamond anvil cell at high pressure and temperature. *Rev. Sci. Instrum.* **84,** 025118–025119 (2013).
20. Marquardt, H. *et al.* Elastic shear anisotropy of ferropericlase in Earth's lower mantle. *Science* **324,** 224–226 (2009).
21. Cordier, P., Amodeo, J. & Carrez, P. Modelling the rheology of MgO under Earth's mantle pressure, temperature and strain rates. *Nature* **481,** 177–180 (2012).
22. Wentzcovitch, R. M. *et al.* Anomalous compressibility of ferropericlase throughout the iron spin cross-over. *Proc. Natl Acad. Sci. USA* **106,** 8447–8452 (2009).
23. Morra, G. *et al.* The fate of the slabs interacting with a density/viscosity hill in the mid-mantle. *Phys. Earth Planet. Inter.* **180,** 271–282 (2010).
24. Ribe, N. M., Stutzmann, E., Ren, Y. & van der Hilst, R. Buckling instabilities of subducted lithosphere beneath the transition zone. *Earth Planet. Sci. Lett.* **254,** 173–179 (2007).
25. Van der Hilst, R. D. & Kárason, H. Compositional heterogeneity in the bottom 1000 kilometers of Earth's mantle: Toward a hybrid convection model. *Science* **283,** 1885–1888 (1999).
26. Becker, T. W. & Boschi, L. A comparison of tomographic and geodynamic mantle models. *Geochem. Geophys. Geosyst.* **3,** 1003 (2002).
27. Houser, C. & Williams, Q. The relative wavelengths of fast and slow velocity anomalies in the lower mantle: Contrary to the expectations of dynamics? *Phys. Earth Planet. Inter.* **176,** 187–197 (2009).
28. Cammarano, F., Marquardt, H., Speziale, S. & Tackley, P. J. Role of iron-spin transition in ferropericlase on seismic interpretation: A broad thermochemical transition in the mid mantle? *Geophys. Res. Lett.* **37,** L03308 (2010).
29. Merkel, S. *et al.* Deformation of (Mg$_{0.9}$Fe$_{0.1}$)SiO$_3$ Perovskite aggregates up to 32 GPa. *Earth Planet. Sci. Lett.* **209,** 351–360 (2003).
30. Mitrovica, J. X. & Forte, A. M. A new inference of mantle viscosity based upon joint inversion of convection and glacial isostatic adjustment data. *Earth Planet. Sci. Lett.* **225,** 177–189 (2004).

Author contributions

Both authors contributed equally to the design and execution of this research and wrote the paper.

Competing financial interests

The authors declare no competing financial interests.

evidence of wind abrasion in the northern canyons — such as streamlined ridges of ignimbrite in the lee of boulders — supports this interpretation. The Puripicar canyons demonstrate that, under the right conditions, wind can enhance bedrock canyon incision.

Given this terrestrial evidence of wind's erosional potential, Perkins and colleagues propose that canyons on Mars may also have been modified by the wind. However, that is not to suggest that the Martian canyons were carved entirely by wind, and without water. Even in the Puripicar channels, wind and water have shared erosional duties. Furthermore, Martian canyons do not occur in straight, parallel arrays like those in the Puripicar, and it is unlikely that wind could create the sinuous channels or networks of tributaries that are observed on the Martian surface. Nevertheless, the cumulative effect of billions of years of wind erosion on canyon morphology could be significant. Longitudinal profiles could have been streamlined, and cross-sectional dimensions changed. Some canyons might have been altered beyond recognition as fluvial landforms.

The implications of wind-driven canyon incision extend beyond Earth and Mars to other planetary bodies with atmospheres. Saturn's moon Titan, with its icy landscapes and hydrocarbon rivers, has prominent canyons and strong evidence for wind activity in the form of extensive dune fields. Perhaps Titan's river canyons have also been abraded by wind.

The potential imprint of wind on fluvial landforms complicates hydrologic and climatic interpretations based on landscape morphology. Without knowing more about the dynamics of wind abrasion in canyons, it is difficult to estimate the wind-induced modification of a specific landform. Additional research will be required to understand how wind patterns, canyon geometry, sand supply and rock properties control the abrasion rate. More work is also needed to determine how three-dimensional wind flow drives erosional mechanisms that extend canyons downwind, as opposed to creating unconnected, streamlined forms. Such advances would help constrain the contribution of wind action to a canyon's form.

Perkins et al.[4] show that wind can modify and extend bedrock canyons, as demonstrated in the northern Chilean Andes. Future interpretations of planetary landscapes where wind is a dominant surface process will need to take this mechanism into account. ❏

J. Taylor Perron is in the Department of Earth, Atmospheric and Planetary Sciences, Massachusetts Institute of Technology, Cambridge, Massachusetts 02139, USA. e-mail: perron@mit.edu

References
1. Grotzinger, J. P. et al. Science **343**, 6169 (2014).
2. Anderson, R. B. & Bell, J. F. III Mars J. **5**, 76–128 (2010).
3. Baker, V. R. Nature **412**, 228–236 (2001).
4. Perkins, J. P., Finnegan, N. J. & de Silva, S. L. Nature Geosci. **8**, 305–310 (2015).
5. Perron, J. T., Richardson, P. W., Ferrier, K. L. & Lapôtre, M. Nature **492**, 100–103 (2012).
6. Ferrier, K. L., Huppert, K. L. & Perron, J. T. Nature **496**, 206–209 (2013).
7. Irwin, R. P. III & Howard, A. D. J. Geophys. Res. **107**, 5056 (2002).
8. Craddock, R. A. & Howard, A. D. J. Geophys. Res. **107**, 5111 (2002).
9. Bridges, N. et al. Nature **485**, 339–342 (2012).

GEODYNAMICS

Strength under pressure

Subducting oceanic crust is sometimes observed to stagnate in the lower mantle. Laboratory experiments show that high pressures in the deep Earth may strengthen mantle rocks, increasing their viscosity and halting the sinking slabs.

Patrick Cordier

Beneath Indonesia, the dense cold Indo–Australian plate sinks into the mantle. Seismic data provide images of the progression of the subducting slab and show that it penetrates well into Earth's lower mantle. However on the western side of the arc, at about 1,000 km depth, the slab broadens and seems to stagnate[1]. Other slabs also stagnate during their descent through Earth's lower mantle, yet there are no known structural or compositional changes that might cause the slabs to stall at this depth. Writing in *Nature Geoscience*, Marquardt and Miyagi[2] propose that pressure-induced strengthening of the common mantle mineral ferropericlase increases the viscosity of mantle rocks surrounding the subducting slabs, preventing the slabs from sinking further.

Earth's mantle is made of solid rocks. However, on long timescales the mantle flows at extremely slow rates and transports heat from the core towards the surface.

This upwards convecting flux is balanced by the downwards flux of cold, dense slabs of oceanic lithosphere. The rate of slab descent depends on many factors including the density difference between the slab and the surrounding mantle, and the ability of mantle rocks to flow to let the slab pass through. Measuring the sinking velocities of slabs shows that the lower mantle, which begins at about 660 km depth, is between 1 to 3 orders of magnitude more viscous than the upper mantle[3].

Under the increasing influence of pressure, mineral phases in the upper mantle transform into more compact structures. In particular, olivine converts into denser wadsleyite and ringwoodite at 410 and 520 km depth, respectively, and all minerals transform into a mixture of bridgmanite and ferropericlase at 670 km depth. These changes in mineral structure have been identified within the Earth using seismic data, because the speed of seismic waves

changes as they pass through minerals with different structures. However, no changes in seismic velocity are observed, and thus no other mineral phase transitions are known to occur until about 2,900 km depth, close to the boundary between the core and mantle. It is therefore unclear why some slabs stagnate at about 1,000 km depth.

Marquardt and Miyagi[2] used high-pressure laboratory experiments to assess the rheology of the mineral ferropericlase, which makes up about 20% of the lower mantle. They compressed samples of ferropericlase under almost 100 GPa of pressure using a diamond anvil cell and found that the strength of ferropericlase increased by a factor of three at pressures equivalent to depths of 600 to 2,000 km in the Earth. Under such high pressures the mineral volume decreases by about 20% (Fig. 1), ionic bonds between the atoms are strengthened, and the mineral becomes three times less compressible[4]. The authors
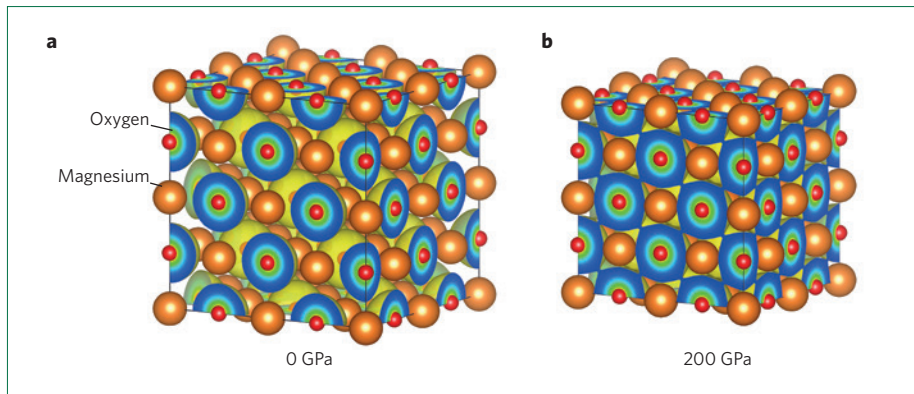
Figure 1 | Electronic structure of magnesium oxide. **a,b,** Much of the lower mantle is composed of magnesium oxide in the form of ferropericlase (**a**), which compresses under high pressure (**b**). The electronic structure of MgO shown here was calculated using first-principles. Marquardt and Miyagi[2] show that under high pressures, equivalent to about 1,000 km depth in the lower mantle, ferropericlase compresses and the bonds between the atoms are strengthened. This change in electronic structure causes a dramatic increase in the strength and viscosity of the lower mantle, so inhibits the descent of subducting slabs, causing them to stall. Figure courtesy of Ph. Carrez, Université Lille 1.

model the experimental data and suggest that this increase in strength correlates to an increase of 2.3 orders of magnitude in the viscosity of the mantle at about 900 km depth. The highly viscous nature of the mantle at these depths would resist slab descent, causing the slabs to stagnate.

The observed change in properties of ferropericlase forces us to reconsider our thoughts on mantle rheology. Previously, we have relied on seismological observations of discontinuities to infer the evolution of properties in the mantle. The current work shows that changes can occur in the deep mantle without creating any sharp seismic boundaries. The result also raises questions about how these pressure-induced changes may affect global convection. For example, slab stagnation provides a mechanism to create distinct geochemical reservoirs in the deep mantle that might remain unmixed for very long-periods of time.

The experiments identify fundamental changes in the electronic structure of matter under pressure. Of course, many questions remain. In addition to ferropericlase, the lower mantle is largely composed of bridgmanite. The response of bridgmanite to pressure is thus pivotal for understanding the resistance of the mantle to slab penetration and should be addressed as a priority. There are also some intrinsic limitations of high-pressure deformation experiments. Marquardt and Miyagi's experiments were conducted at room temperature so cannot account for complex deformation mechanisms involving diffusion that may occur under the high temperatures of Earth's interior. Natural strain rates are also difficult to reproduce under experimental conditions, and these may also affect the deformation mechanisms[5].

Marquardt and Miyagi[2] show that an increase in the viscosity of lower-mantle minerals that is invisible to seismic probing could cause subducting slabs to stagnate during their descent into the deep Earth. The result highlights a fundamental change in the electronic structure of minerals in the Earth's lower mantle and implies that mantle rheology might be much more complex and exciting than previously thought. ❐

Patrick Cordier is in the Unité Matériaux et Transformations, Université Lille 1, CNRS UMR 8207, F-59650 Villeneuve d'Ascq, France.
e-mail: patrick.cordier@univ-lille1.fr

References
1. Fukao, Y. & Obayashi, M. *J. Geophys. Res.* **118,** 5920–5938 (2013).
2. Marquardt, H. & Miyagi, L. *Nature Geosci.* **8,** 311–314 (2015).
3. Butterworth, N. P. *et al. J. Geodynam.* **73,** 1–13 (2014).
4. Marquardt, H., Speziale, S., Reichmann, H. J., Frost, D. J. & Schilling, F. R. *Earth Planet. Sci. Lett.* **287,** 345–352 (2009).
5. Cordier, P., Amodeo, J. & Carrez, P. *Nature* **481,** 177–180 (2012).

PLANETARY SCIENCE

Iron fog of accretion

Pinpointing when Earth's core formed depends on the extent of metal–silicate equilibration in the mantle. Vaporization and recondensation of impacting planetesimal cores during accretion may reconcile disparate lines of evidence.

William W. Anderson

Formation and growth of the core played a critical part in early Earth's evolution. Yet the timing and duration of core formation remain uncertain because the degree of chemical equilibration that occurred between metal and silicate materials as accretion progressed is poorly constrained. Isotopic and geochemical constraints[1,2] indicate that substantial equilibration may have taken place,

but dynamical studies[3,4] suggest that a high degree of equilibration is unlikely because of the intimate physical mixing of metal and silicate required. Writing in *Nature Geoscience*, Kraus *et al.*[5] present experimental evidence that the shock pressures produced by impacts during accretion could have vaporized the iron cores of differentiated planetesimals and enhanced metal–silicate mixing.

Hafnium–tungsten chronometry, based on the decay of ^{182}Hf to ^{182}W, is particularly well suited for constraining the timing of core formation. Tungsten is a siderophile element that tends to enter the metal phase, whereas hafnium is a lithophile element that would have partitioned into silicates during Earth's differentiation. Thus, any ^{182}W found in the bulk silicate Earth — comprising the crust and mantle — should

Slab stagnation in the shallow lower mantle linked to an increase in mantle viscosity

Hauke Marquardt and Lowell Miyagi

Starting material:

The starting materials were finely-ground powders of $(Mg_{0.9}Fe_{0.1})O$ and $(Mg_{0.8}Fe_{0.2})O$. The powders were made from stoichiometric mixtures of reagent grade MgO and Fe_2O_3 treated in a gas-mixing furnace at 1250°C at an oxygen fugacity 2 log units below the fayalite magnetite oxygen buffer. A small amount of fine-powdered platinum was mixed with the sample material to determine pressure in the experimental runs performed in cBN gaskets.

Synchrotron high-pressure x-ray diffraction:

Diamond culet sizes were 300 μm, bevelled to 150 μm. X-rays were focused to about 15 by 15 μm². The x-ray energy was set to 25 keV. Platinum was used as pressure standard employing previously published equation of state parameters[31]. In the experimental run carried out in Be gasket, pressure was determined from the unit cell volume of (Mg,Fe)O using our experimental data collected in cBN gasket on the same sample material as reference. Pressure was increased using a gas-membrane system. In the two experimental runs using cBN gaskets, pressure was increased in small pressure steps (about 1 GPa) with an average compression rate of ~10-14 GPa/h. In the experiment where a Be gasket was employed, pressure steps were larger (average about 10 GPa) and the average compression rate was ~45 GPa/h. Pressure increase is discontinuous in these experiments and thus strain and strain rate are also discontinuous. Each incremental pressure increase takes about 1 minute. The initial gasket thickness is ~25 μm and is compressed to an estimated thickness of ~10 μm. Based on this, we estimate strain rates to be on the order of $1\cdot10^{-4}$ s^{-1} and $1\cdot10^{-3}$ s^{-1} respectively. The diffraction images were recorded on a MAR 345 image plate, sliced in the

Fit2d program[32] and analysed using the program MAUD[33] (Supplementary Fig. 1). The "radial diffraction in the DAC" model[34] was used to fit lattice strains in ferropericlase. The E-WIMW model which is similar to the WIMV model[35], but allows for incomplete and arbitrary pole figure coverage was employed to fit textures. Cylindrical symmetry was imposed. The orientation distribution function (ODF) was exported to BEARTEX[36] and was smoothed with a 10° Gauss filter. The maximum of the ODF as a function of pressure is shown in Supplementary Fig. 2. The unit cell volumes that we obtained from our rXRD experiments are generally consistent with previously determined data and indicate that the iron spin crossover took place above 50 GPa for $(Mg_{0.9}Fe_{0.1})O$ and above 60 GPa for $(Mg_{0.8}Fe_{0.2})O$ in cBN gaskets (Supplementary Fig. 3).

Viscosity calculation in high strain areas:

We use our experimental data to calculate viscosities for $(Mg_{0.8}Fe_{0.2})O$ ferropericlase and $MgSiO_3$ bridgmanite, and a mixture of the two under conditions of dislocation creep, which is likely the dominant deformation mechanism in high strain areas of the lower mantle[37]. To scale our low temperature measurements to high temperature viscosity we use a previously developed and tested formulation[38]. Strain rate ($\dot{\varepsilon}$) is given by

$$\dot{\varepsilon} = A' \frac{D_L \tau_p \boldsymbol{b}}{kT} \left(\frac{\sigma}{\tau_p} \right)^n \tag{1}$$

and

$$A' = 0.1 \left(\frac{\tau_p}{G} \right)^2 \tag{2}$$

2

where A' is a pre-exponential factor, D_L is the lattice diffusion coefficient of the slowest species, τ_p is Peierls stress, $\boldsymbol{b}$ is Burgers vector, k is Boltzman's constant, T is temperature, σ is stress, n is the stress exponent and G is the shear modulus.

To determine the diffusion coefficients D_L at high temperature and pressure we use a homologous temperature scaling law, where D_L (P,T) is defined as

$$D_L(P,T) = D_0 \exp\left(-\frac{gT_m(P)}{T}\right)$$

(3)

The pre-exponential factor D_0 is a constant and $T_m(P)$ is the melting temperature at a given pressure, g is a dimensionless constant given by

$$g = H^*(P)/RT_m(P)$$

(4)

$H^*(P)$ is the activation enthalpy at a given pressure and R is the gas constant.

To calculate viscosity (μ) from equation (1) we use the relationship

$$\mu = \frac{\sigma}{2\dot{\varepsilon}}$$

(5)

To obtain bulk viscosities of a two phase aggregate of MgSiO$_3$ bridgmanite and ferropericlase, we use the approach of ref. 13. Since we are concerned with viscosities in high strain regions, such as in regions near subducting slabs, we calculate viscosities for an interconnected weak layer type structure (IWL)[13,37,39].

3

For an IWL structure the normalized viscosity μ^* is given by

$$\mu^* = \frac{[a^2 - 2a(a-1)\phi_1 + (a-1)^2 \phi_1{}^2]b}{a^2 - (b-a^2)\phi_1} \tag{6}$$

where

$$\mu^* = \mu/\mu_1 \tag{7}$$

$$a = \gamma_2/\gamma_1 \tag{8}$$

$$b = \mu_2/\mu_1 \tag{9}$$

Where μ is the bulk viscosity of the two-phase continuum, γ is the density of a phase, ϕ is the volume fraction of a phase and the subscripts 1 and 2 indicate the weaker phase and stronger phase respectively. We note that eq. 6 was derived assuming linear rheology (Newtonian), whereas we assume non-linear rheology for both bridgmanite and ferropericlase. However, for our calculation of the aggregate viscosity in IWL structure, a constant stress assumption (throughout the aggregate) applies, which allows for applying eq. 6 to derive an aggregate viscosity but at a certain stress. In the future, our data could serve as input parameters for more sophisticated numerical modelling of the deformation behaviour of a two-phase assemblage[40].

Parameterization of viscosity calculation:

Supplementary Table 1 summarizes the employed parameters used to calculate lower mantle viscosities along a typical lower mantle geotherm[41]. We varied the input parameters over a

4

wide range of values (Supplementary Tab. 1). We found that the absolute numbers of mantle viscosities depend strongly on the values of the input parameters. In contrast, the change of viscosity in the upper 900 km of the lower mantle is always between 2 and 2.5 orders of magnitude and is therefore a very robust finding (Supplementary Tab. 1). Calculations were performed for single-phase ferropericlase with a typical lower mantle composition of $(Mg_{0.8}Fe_{0.2})O$ and $MgSiO_3$ bridgmanite. Lower mantle viscosities in large strain regions were then derived from the single-phase viscosities assuming a lower mantle assemblage of 80% by volume of $MgSiO_3$ and 20% by volume of $(Mg_{0.8}Fe_{0.2})O$. Calculated viscosities are shown in Supplementary Fig. 4.

Burgers vector b: We use <110> for $MgSiO_3$ bridgmanite[42] and 1/2<110> for ferropericlase[43]. We use high-pressure single-crystal x-ray diffraction compression data of iron-bearing $MgSiO_3$ (ref. 44) along with computed linear thermal expansion coefficients[45] to calculate the variation in length of the burgers vector along a geotherm[41].

Peierls stress τ: We assume that values of flow strength derived from rXRD experiments at high-pressure and 300 K can be used to approximate the value of the Peierls stress[46,47]. We used data for $(Mg_{0.8}Fe_{0.2})O$ from our experiments to 96 GPa and employed a linear extrapolation of our data above 65 GPa to cover the pressure range to 136 GPa. For $MgSiO_3$ bridgmanite, we employed previously published data to 32 GPa (ref. 29), extrapolated by using either a linear or exponential function.

Stress exponent n: We use n = 3.5 for $MgSiO_3$ bridgmanite based on creep experiments of analogue materials (e.g. ref. 48) and n = 4 for ferropericlase[43].

Shear modulus G: The values for the shear modulus along the geotherm were taken from recent computational studies on $MgSiO_3$ (ref. 49) and $(Mg_{0.79}Fe_{0.21})O$ (ref. 50).

5

Lattice diffusion coefficient D_L (P,T): Lattice diffusion of Si should control creep in $MgSiO_3$ bridgmanite as it is typically the slowest diffusing species in silicates[3]. To derive $D_L(P,T)$ for $MgSiO_3$ bridgmanite, we use the pre-exponential factor for Si diffusion in $MgSiO_3$ from ref. 51 (D_0=2.7x 10^{-10}m^2/s), a constant $g = 14$ (ref. 51) and previously published data for $T_{m,PV}(P)$ (ref. 52). We tested a wide range of published melting curves for bridgmanite[53-55], but effects on calculated viscosities for the two-phase assemblage are negligible (<0.1 Log units at 700 km depth). The diffusion of oxygen should be the appropriate diffusion coefficient for dislocation creep[56] in (Mg,Fe)O. To derive $D_L(P,T)$ for $(Mg_{0.8}Fe_{0.2})O$, we use the pre-exponential factor D_0 for O self-diffusion in MgO (D_0=9.05 x 10^{-8} m^2/s) (ref. 57). The constant $g = 11$ was derived from equation (4), where the activation enthalpy H of MgO at 0 GPa was taken from a computational study[57]. The room pressure melting temperature $T_{m,FP}$ (0 GPa) was assumed to be 2508 K for $(Mg_{0.8}Fe_{0.2})O$ based on experimental work[58]. The range of tested values for g (Supplementary Tab. 1) accounts for variations in published H-values between recent theoretical studies[57,59,60] and an assumed uncertainty of the $T_{m,FP}$ (0 GPa) of $\pm$ 200 K. $T_{m,FP}(P)$ was derived from the melting curve of MgO (ref. 61), where correction for 20% at. Fe was done by multiplying $T_{mMgO}(P)$ with 0.75 based on high-pressure melting experiments on (Mg,Fe)O (ref. 58).

Density contrast α: The density contrast between bridgmanite and ferropericlase along a geotherm was derived from recent computational data[50] for $(Mg_{.79}Fe_{.21})O$ and iron-bearing bridgmanite[62].

Stress σ: For an IWL microstructure an iso-stress condition applies. We assume a stress range of 5-20 MPa, on the order of stresses where a transition from diffusion to dislocation creep should occur in the lower mantle[56].

6

Modelling the potential effect of the iron spin crossover on the viscosity structure of the lower mantle:

The potential effect of the iron spin crossover on oxygen diffusivities in ferropericlase was modelled by assuming that the increase of diffusion rates directly scales with the decrease of bulk modulus and reaches a maximum when the bulk modulus has its lowest value. We assumed that diffusion is enhanced by a factor of 11-30 (ref. 63). The depth-dependent bulk modulus was taken from an experimental study[64]. Results are shown in Supplementary Fig. 4.

Viscosity calculation in low strain areas:

The "background viscosity" μ in low strain areas was calculated assuming deformation by diffusion creep, where the viscosity is given by[3]

$$\frac{1}{\mu} = A \frac{\Omega}{RT} \frac{D_{eff}}{h}$$

(10)

with the constant $A = 13.3$ (ref. 3), the molar volume Ω, the gas constant R, absolute temperature T, and effective diffusion coefficient D_{eff}, and grain size h. Parameters were the same as for the calculation of viscosity in high strain areas. The grain size was chosen to vary between 0.1 and 1 mm according to ref. 65. We further assume that D_{eff} is equivalent to the lattice diffusion coefficient for each phase as lattice diffusion coefficients control diffusion creep according to ref. 3. Our results for the "background viscosity" are in general agreement with the viscosities estimated based on first-principle calculations of diffusion rates in silicate perovskite[4].

To obtain bulk viscosities of a two phase aggregate of $MgSiO_3$ bridgmanite and ferropericlase, we again use the approach of ref. 13. Here, we are concerned with viscosities

7

in low strain regions and, accordingly, we calculate viscosities for a load-bearing framework type structure (LBF) by using the identity:

$$\mu^* = (1 - b)\phi_1 + b \tag{11}$$

8
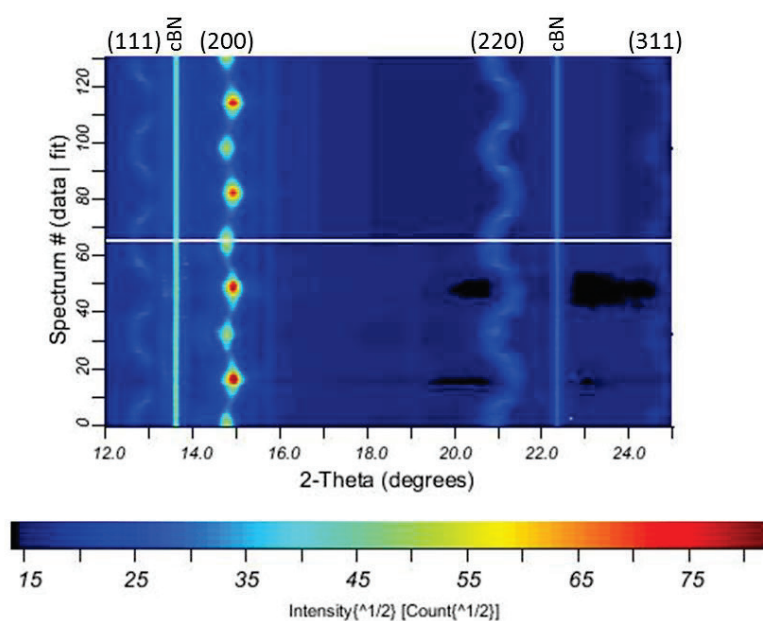
Supplementary Figure 1. MAUD analysis of data collected on (Mg$_{0.8}$Fe$_{0.2}$)O at 75.6 GPa in cBN. Lower half shows collected data, upper half corresponds to the respective fit. Corresponding lattice planes of (Mg$_{0.8}$Fe$_{0.2}$)O are labelled
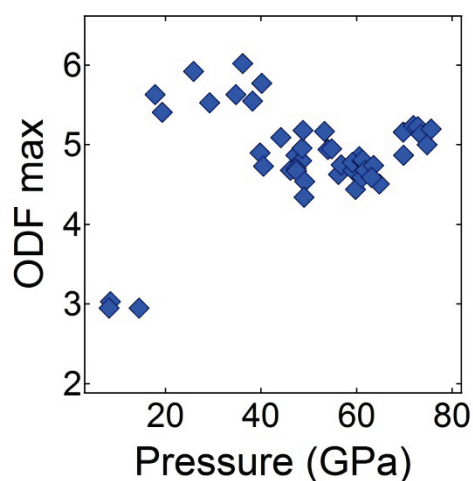

Supplementary Figure 2. Maximum of orientation distribution function of (Mg$_{0.8}$Fe$_{0.2}$)O in cBN gasket. Upon initial pressure increase, the texture strength (maximum in orientation distribution function ODF) increases with pressure and saturates above 20 GPa. At 40 GPa, the ODF max drops.

9
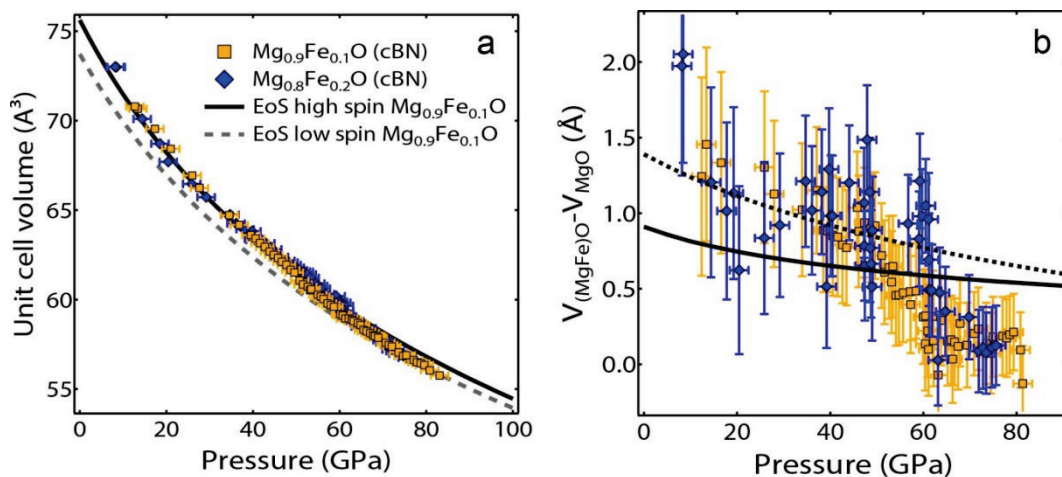
Supplementary Figure 3. Unit cell volumes of (Mg,Fe)O measured in cBN gaskets as a function of pressure. (a) Curves for high-spin and low-spin ferropericlase are calculated using previously reported equation of state parameters (ref. 18). (b) Deviation between measured unit cell volumes of (Mg,Fe)O in cBN gaskets and MgO. Blue diamonds: $(Mg_{0.8}Fe_{0.2})O$; orange squares: $(Mg_{0.9}Fe_{0.1})O$. Uncertainties are based on an assumed uncertainty in pressures of 2 GPa. The solid and dashed lines indicate the expected behaviors of high-spin $(Mg_{0.9}Fe_{0.1})O$ (ref. 18) and $(Mg_{0.83}Fe_{0.17})O$ (ref. 66).
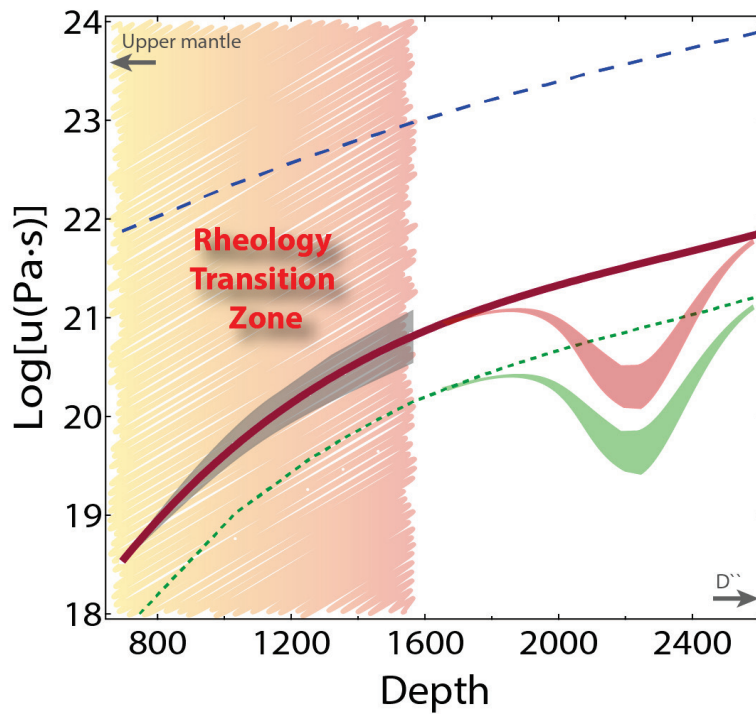
Supplementary Figure 4. Calculated viscosity profiles in high strain areas along a geotherm (ref. 41). Bridgmanite (blue dashed curve), ferropericlase (green dotted curve) and a typical lower mantle assemblage of 80% by volume of bridgmanite and 20% by volume of ferropericlase (red solid curve). The grey shaded region indicates the uncertainties in our viscosity calculations for a lower mantle assemblage assuming a fixed viscosity value at 700 km depth. The hatched region corresponds to the pressure range where the rheology transition in ferropericlase was observed in our experiments. The shaded regions illustrates a potential decrease of viscosities related to enhanced element diffusion rates caused by the iron spin crossover in ferropericlase (refs. 22,63).

Supplementary Table 1. Parameters used for viscosity calculation. The values given correspond to the values used for Fig. 3 of the main paper. The effects of variations in input parameters on the absolute value of viscosity at a depth of 700 km and the change of viscosity to a depth of 1560 km are summarized.

Parameter	Value	Range of input parameters		Increase of Log(μ) from 700 km to 1560 km depth		Log(μ) at 700 km depth	
		min	max	min	max	min	max
φ	0.2	0.1	0.3	2.3	2.3	18.4	18.8
b_{Pv}	$6.x \times 10^{-10}$ m	-30%	+30%	2.3	2.3	18.5	18.5
b_{Fp}	$5.x \times 10^{-10}$ m	-30%	+30%	2.3	2.3	18.5	18.5
τ_{pv}	exp. fit	exp. extrapol.	lin. extrapol.	2.3	2.3	18.5	18.5
n_{Pv}	3.5	3	4	2.3	2.3	18.5	18.5
n_{Fp}	4	3.5	4.5	2	2.5	17.3	19.8
G_{Pv}	100-300 GPa	-30%	+30%	2.3	2.3	18.5	18.5
G_{Fp}	100-300 GPa	-30%	+30%	2.3	2.3	18.2	18.8
$D0_{Pv}$	2.70E-10 m^2/s	2.70E-11 m^2/s	2.70E-09 m^2/s	2.3	2.3	18.5	18.5
$D0_{Fp}$	9.05E-08 m^2/s	9.05E-09 m^2/s	9.05E-07 m^2/s	2.3	2.3	17.5	19.5
g_{Pv}	14	12	16	2.3	2.3	18.5	18.5
g_{Fp}	11	9	13	2	2.5	16.8	20.3
$T_{m,PV}(P)$	3700-5500K	-500K	+500K	2.3	2.3	18.5	18.5
$T_{m,FP}(P)$	$T_{m,MgO}(P) \times 0.75$	$T_{m,MgO}(P) \times 0.6$	$T_{m,MgO}(P) \times 0.9$	2	2.5	16.8	20.3
α	0.92-1.03	-30%	+30%	2.3	2.3	18.3	18.7
σ	10 MPa	5 MPa	20 MPa	2.3	2.3	17.5	19.3

References Supplementary Information

31   Fei, Y. *et al.* High-Pressure Geoscience Special Feature: Toward an internally consistent pressure scale. *Proc. Natl. Acad. Sci.* **104**, 9182-9186 (2007).

32   Hammersley, A. P., Svensson, S. O., Hanfland, M., Fitch, A. N. & Hausermann, D. Two-dimensional detector software: From real detector to idealised image or two-theta scan. *High Press. Res.* **14**, 235-248 (1996).

33   Lutterotti, L., Matthies, S., Wenk, H.-R., Schultz, A. S. & Richardson, J. W. Combined texture and structure analysis of deformed limestone from time-of-flight neutron diffraction spectra. *J. Appl. Phys.* **81**, 594-600 (1997).

34   Singh, A. K., Balasingh, C., Mao, H.-k., Hemley, R. J. & Shu, J. Analysis of lattice strains measured under nonhydrostatic pressure. *J. Appl. Phys.* **83**, 7567-7575 (1998).

35   Matthies, S. & Vinel, G. W. On the Reproduction of the Orientation Distribution Function of Texturized Samples from Reduced Pole Figures Using the Conception of a Conditional Ghost Correction. *Phys. Status Solidi B* **112**, K111-K114 (1982).

36   Wenk, H. R., Matthies, S., Donovan, J. & Chateigner, D. BEARTEX: a Windows-based program system for quantitative texture analysis. *J. Appl. Crystallogr.* **31**, 262-269 (1998).

37   McNamara, A. K., Karato, S.-I. & van Keken, P. E. Localization of dislocation creep in the lower mantle: implications for the origin of seismic anisotropy. *Earth Planet. Sci. Lett.* **191**, 85-99 (2001).

38   Wang, J. N. & Nieh, T. G. Role of Peierls stress in power law dislocation creep. *Mater Sci Eng A* **202**, 52-56 (1995).

39   Wang, Y. *et al.* In situ high-pressure and high-temperature X-ray microtomographic imaging during large deformation: A new technique for studying mechanical behavior of multiphase composites. *Geosphere* **7**, 40-53 (2011).

40   Madi, K., Forest, S., Cordier, P. & Boussuge, M. Numerical study of creep in two-phase aggregates with a large rheology contrast: implications for the lower mantle. Earth Planet. Sci. Lett. 237, 223-238 (2005).

41   Brown, J. M. & Shankland, T. J. Thermodynamic parameters in the Earth as determined from seismic profiles. *Geophys. J. Roy. Astr. S.* **66**, 579-596 (1981).

42   Miyajima, N., Yagi, T. & Ichihara, M. Dislocation microstructures of $MgSiO_3$ perovskite at a high pressure and temperature condition. *Phys. Earth Planet. Inter.* **174**, 153-158 (2009).

43   Stretton, I., Heidelbach, F., Mackwell, S. & Langenhorst, F. Dislocation creep of magnesiowüstite ($Mg_{0.8}Fe_{0.2}O$). *Earth Planet. Sci. Lett.* **194**, 229-240 (2001).

44   Boffa-Ballaran, T. B. *et al.* Effect of chemistry on the compressibility of silicate perovskite in the lower mantle. *Earth Planet. Sci. Lett.* **333–334**, 181-190 (2012).

45   Wen, B., Shao, T., Melnik, R., Kawazoe, Y. & Tian, Y. Temperature and pressure dependent geometry optimization and elastic constant calculations for arbitrary symmetry crystals: Applications to MgSiO3 perovskites. *J. Appl. Phys.* **113**, - (2013).

46   Karato, S.-I. *Deformation of Earth Materials: Introduction to the Rheology of Solid Earth*. Cambridge University Press, 2008.

47   Gleason, A. E. & Mao, W. L. Strength of iron at core pressures and evidence for a weak Earth's inner core. *Nature Geosci* **6**, 571-574 (2013).

48   Wang, Z., Karato, S.-i. & Fujino, K. High temperature creep of single crystal strontium titanate ($SrTiO_3$): a contribution to creep systematics in perovskites. *Phys. Earth Planet. Inter.* **79**, 299-312 (1993).

49   Wentzcovitch, R. M., Karki, B. B., Cococcioni, M. & de Gironcoli, S. Thermoelastic Properties of $MgSiO_3$-Perovskite: Insights on the Nature of the Earth's Lower Mantle. *Phys. Rev. Lett.* **92**, 018501 (2004).

50   Wu, Z., Justo, J. F. & Wentzcovitch, R. M. Elastic Anomalies in a Spin-Crossover System: Ferropericlase at Lower Mantle Conditions. *Phys. Rev. Lett.* **110**, 228501 (2013).

51   Yamazaki, D., Kato, T., Yurimoto, H., Ohtani, E. & Toriumi, M. Silicon self-diffusion in $MgSiO_3$ perovskite at 25 GPa. *Phys. Earth Planet. Inter.* **119**, 299-309 (2000).

52   Akins, J. A., Luo, S.-N., Asimow, P. D. & Ahrens, T. J. Shock-induced melting of $MgSiO_3$ perovskite and implications for melts in Earth's lowermost mantle. *Geophys. Res. Lett.* **31**, L14612 (2004).

53   Stixrude, L. & Karki, B. Structure and Freezing of $MgSiO_3$ Liquid in Earth's Lower Mantle. *Science* **310**, 297-299 (2005).

54   Wang, Z. W. The melting of Al-bearing perovskite at the core–mantle boundary. *Phys. Earth Planet. Inter.* **115**, 219-228 (1999).

55   Belonoshko, A. B. *et al.* High-Pressure Melting of $MgSiO_3$. *Phys. Rev. Lett.* **94**, 195701 (2005).

56   Van Orman, J. A., Fei, Y., Hauri, E. H. & Wang, J. Diffusion in MgO at high pressures: Constraints on deformation mechanisms and chemical transport at the core-mantle boundary. *Geophys. Res. Lett.* **30**, 1056 (2003).

57   Ito, Y. & Toriumi, M. Pressure effect of self-diffusion in periclase (MgO) by molecular dynamics. *J. Geophys. Res.* **112**, B04206 (2007).

58   Zhang, L. & Fei, Y. Melting behavior of (Mg,Fe)O solid solutions at high pressure. *Geophys. Res. Lett.* **35**, L13302 (2008).

59   Karki, B. B. & Khanduja, G. Vacancy defects in MgO at high pressure. *Am. Mineral.* **91**, 511-516 (2006).

60   Ita, J. & Cohen, R. E. Effects of Pressure on Diffusion and Vacancy Formation in MgO from Nonempirical Free-Energy Integrations. *Phys. Rev. Lett.* **79**, 3198-3201 (1997).

61   Alfè, D. Melting Curve of MgO from First-Principles Simulations. *Phys. Rev. Lett.* **94**, 235701 (2005).

62   Tsuchiya, T. & Wang, X. Ab initio investigation on the high-temperature thermodynamic properties of Fe^{3+}-bearing $MgSiO_3$ perovskite. *J. Geophys. Res.* **118**, 83-91 (2013).

63   Saha, S., Bengtson, A. & Morgan, D. Effect of anomalous compressibility on Fe diffusion in ferropericlase throughout the spin crossover in the lower mantle. *Earth Planet. Sci. Lett.* **362**, 1-5 (2013).

64   Mao, Z., Lin, J.-F., Liu, J. & Prakapenka, V. B. Thermal equation of state of lower-mantle ferropericlase across the spin crossover. *Geophys. Res. Lett.* **38**, L23308 (2011).

65   Solomatov, V. S., El-Khozondar, R. & Tikare, V. Grain size in the lower mantle: constraints from numerical modeling of grain growth in two-phase systems. *Phys. Earth Planet. Inter.* **129**, 265-282 (2002).

66   Speziale, S. *et al.* Effects of Fe spin transition on the elasticity of (Mg,Fe)O magnesiowüstite and implications for the seismological properties of the Earth's lower mantle. *J. Geophys. Res.* **112** (2007).